Molecular Dynamics Simulation Study of Poly(γ-benzyl L-glutamate) in Dimethylformamide

J. Helfrich, R. Hentschke,* and U. M. Apel

Max-Planck-Institut für Polymerforschung, Postfach 3148, 55021 Mainz, Germany

Received August 23, 1993®

ABSTRACT: We report on atomistic molecular dynamics simulations of poly(γ-benzyl L-glutamate) (PBLG) in dimethylformamide (DMF), where the focus is on the structure and dynamics of the backbone–side chain–solvent interface as well as on the elastic properties of the isolated PBLG molecule. The characterization of the complex backbone–side chain–solvent interface in terms of molecular and atomic radial density and order parameter profiles together with azimuthal pair correlation functions reveals a pronounced solvation shell structure. The range of the induced solvent structure correlates well with the 30-Å effective diameter obtained from light scattering experiments, indicating the importance of including the solvation zone in the molecular excluded volume. We also simulate the isolated PBLG molecule under axial tension and compression and discuss the effect of the solvent on the stability of the helical structure of the backbone. Finally, we calculate the persistence length using a simple extrapolation scheme to construct high molecular weight fragments of the helical backbone based on the simulation trajectory. Our value of 1000 ± 50 Å is well within the range of experimental persistence lengths reported for this system.

Introduction

Solutions of poly(γ-benzyl glutamate) (PBG) are frequently studied systems in the context of the statistical mechanics of flexible chain molecules. Numerous experimental and theoretical studies have focused on PBG in connection with its liquid crystalline phase behavior and complex packing in concentrated bulk solutions[1-7] as well as in quasi two-dimensional self-assembled films.[8]

Here we use the molecular dynamics simulation technique to study PBLG in dilute solution, when the intersolute interactions can be neglected. In our simulations we use one type of solvent, dimethylformamide (DMF), which often is the solvent of choice in experimental studies on PBLG solutions in order to avoid association of the solute. The focus of our simulations is on the structure of the backbone–side chain–solvent interface in the PBLG/DMF system and on the longitudinal and transversal elastic properties of PBLG. Both the profile of the PBLG–DMF interface and the elastic properties of PBLG, particularly its persistence length, are important for understanding thermodynamic properties such as solvent–side chain mixing[9] or the formation and stability of orientationally and translationally ordered phases.[10]

In the case of the interface between a flat solid surface and a liquid it is well-known that the surface induces a pronounced solvation shell structure extending several molecular diameters into the liquid. In fact, at these distances it is the perturbation of the solvation shell structure which almost exclusively determines the force between two approaching surfaces.[11] This is also true for the interaction between rodlike macromolecules in solution, as has been shown experimentally, for instance, for aqueous solutions of DNA.[12] Thus, the solvation shell structure is an integral part of a solute molecule and should be included in experimental and theoretical considerations, which depend on the lateral dimension of the particles. In the present study we characterize the backbone–side chain–solvent interface of the PBLG/DMF system in terms of the radial side chain density, the solvent density, and the solvent orientation order parameter profiles. In addition, we calculate atomic pair correlations on cylindrical shells centered on the PBLG backbone as a function of distance from the backbone. We find a pronounced solvation shell structure overlapping with the region occupied by the side chains and extending approximately 15 Å away from the center of the backbone. This range of solute induced order in the surrounding liquid is in close accord with the 30-Å effective diameter of PBLG in DMF assumed previously in the calculation of molecular stiffness based on light scattering experiments.[13] In addition to the structural characterization, we also compare the short time diffusion of the solvent inside and outside the brush of side chains. The marked difference again indicates that the solvent shell acts as an integral part of PBLG in solution.

Our second focus is on elastic properties of the PBG molecule. Here we first study the response of the isolated helix to static tensile and compressive strain in vacuum as well as in DMF. We obtain a value of 34 GPa for the Young's modulus from static energy minimizations, which is above the range of reported values possibly due to the neglect of entropic contributions. A related quantity, which plays a key role in the statistical mechanics of homogeneous bend elastic main chain polymers, is the persistence length, a measure for the molecular stiffness. Because the stiffness of rodlike molecules strongly affects their orientational and translational phase behavior, extensive experimental effort has been devoted to the measurement of the persistence length in many systems. However, the experimental determination of the molecular bending stiffness is usually complicated by various factors like the polydispersity of the sample or the model dependent analysis of the data.[13] Atomistic simulations, on the other hand, allow the direct determination of the persistence length under realistic but well defined conditions. In the present study we apply a simple extrapolation scheme to construct high molecular weight fragments of the helical backbone based on the simulation trajectory of PBLG in DMF, which yields a persistence length of 1000 ± 50 Å at a temperature of 313 K. This number is well within the range 700–1400 Å reported for the persistence length of this system on the basis of light scattering data.[13] It is also worth mentioning that a comparative simulation in vacuum results in a persistence length of about 600 Å, which underscores the importance of including the polymer–solvent interaction in the simulation.

Method

(a) Construction of the Simulation Box. X-ray studies on crystalline samples find that PBLG forms a 18_5 α-helix with an

® Abstract published in *Advance ACS Abstracts*, December 15, 1993.

0024-9297/94/2227-0472$04.50/0

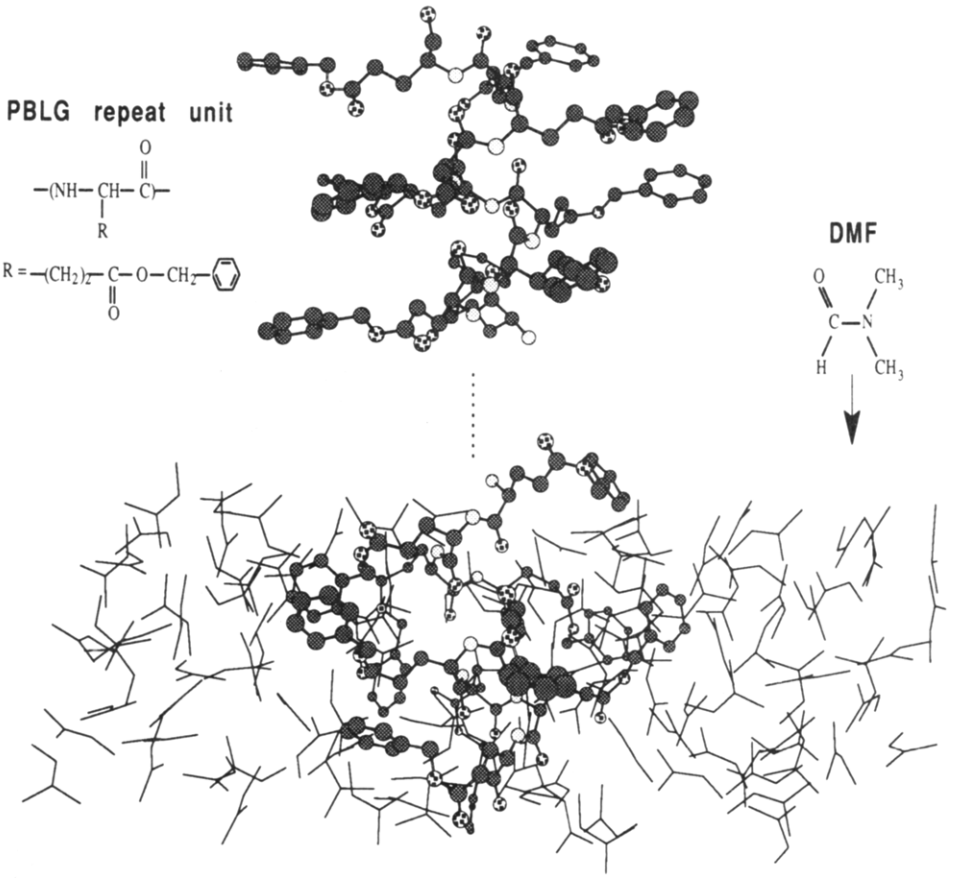

Figure 1. Top: portion of the PBLG segment consisting of nine repeat units. Only the heavy atoms are shown (dark shading, carbon; light shading, nitrogen; dotted, oxygen). Bottom: simulation snapshot showing a small portion of the simulation box containing nine PBLG repeat units including the surrounding solvent.

axial rise per repeat unit (cf. Figure 1) of 1.5 Å and an axial rise per helical turn of 5.4 Å. The helix repeats every 18 residues, which corresponds to 5 turns and a repeat distance of 27.0 Å.[14] There is also indirect evidence based, for instance, on the interpretation of vapor pressure[9] and simultaneous static and dynamic light scattering measurements[13] that the helix conformation is not changed upon dilution in DMF.

For the present simulation we therefore construct a helix segment consisting of 18 repeat units according to the equilibrium bond lengths and valence angles calculated in ref 15 based on the data of Corey and Pauling.[16] The results obtained in ref 15 yield a repeat distance of 26.9 Å, which slightly differs from the 27.0-Å repeat distance obtained from X-ray diffraction studies.[14] After a final geometry optimization of the above PBLG segment using the modeling software INSIGHT[17] we obtain the helix segment used here, which has a repeat distance of 27.04 Å.

This segment of a PBLG molecule is then centered in a simulation box with the volume $V = L_x L_y L_z$, where L_z = 27.04 Å. In order to simulate a quasi infinite helix consisting of periodically repeating segments, it is necessary to introduce covalent bonds between the actual segment and its neighboring periodic images along the z-direction. This is achieved by creating a looping bond between the head and the tail atom of the helical backbone of the segment, which, if the minimum image convention is applied (cf. ref 18), is equivalent to the above covalent bonds.

Whereas the length of the simulation box in the z-direction is defined by the repeat distance of the constructed PBLG helix, the box dimensions along x and y are determined by the range of the PBLG induced solvent structure. In order to be able to achieve bulk behavior of the solvent in the vicinity of the box boundaries, we choose a box whose width exceeds the lateral extension of the PBLG helix with extended side chains by a factor of 3 (cf. below). The solvent is added by placing the DMF molecules on a regular lattice (corresponding to the bulk density ρ_{DMF} = 0.944 g cm^{-3} at 300 K[19]) around the PBLG segment, omitting DMF molecules when their atomic separation from atoms belonging to the PBLG segments is less than 1.2 Å. During the equilibration phase of the subsequent molecular dynamics run we additionally compress the box in the x- and y-directions by 0.1 Å, which yields good agreement with the DMF bulk density near the box boundaries (cf. below). The final simulation box has the lateral dimensions $L_x = L_y$ = 69.3 Å and contains 985 DMF molecules, i.e. a total of 12 342 atoms.

A computer simulation of a system containing such a large number of atoms requires excessive computation time on a workstation. In order to reduce the computational effort we apply the "united atom" model; i.e. explicit CH–, CH_2–, or CH_3– groups are replaced by effective single carbon atoms with a correspondingly increased molar mass and van der Waals radius. Thus, the total number of atoms is decreased to 5231, where now the PBLG segment consists of 306 (united) atoms and each DMF molecule consists of 5 (united) atoms. A schematic illustration of the system is shown in Figure 1.

(b) Simulation Methodology. The MD simulations are based on the numerical integration of Newton's equations of motion

$$m_i \frac{d^2 \vec{x}_i}{dt^2} = -\vec{\nabla}_{\vec{x}_i} V(\vec{x}_1, ..., \vec{x}_n) \tag{1}$$

where i runs over all n (united) atoms in the simulation box. Our simulations are carried out using the molecular mechanics and molecular dynamics modules provided in the AMBER molecular modeling package, where $V(\vec{x}_1, ..., \vec{x}_n)$ is given by

$$V = \sum_{\text{bonds}} f_r (r - r_{\text{equ}})^2 + \sum_{\text{valence angles}} f_\delta (\delta - \delta_{\text{equ}})^2 + \sum_{\text{dihedrals}} f_n [1 + \cos(n\phi - \gamma)] + \sum_{i<j} \left(\frac{A_{ij}}{r_{ij}^{12}} - \frac{B_{ij}}{r_{ij}^{6}} \right) + \sum_{i<j} \frac{q_i q_j}{r_{ij}} + \sum_{\text{H-bonds}} \left(\frac{C_{ij}}{r_{ij}^{12}} - \frac{D_{ij}}{r_{ij}^{10}} \right) \tag{2}$$

$$A_{ij} = \sqrt{\epsilon_i \epsilon_j} (\sigma_i + \sigma_j)^{12}$$

$$B_{ij} = 2\sqrt{\epsilon_i \epsilon_j}(\sigma_i + \sigma_j)^6$$

The first three terms describe bonding interactions (due to bond, valence angle, and dihedral deformations). The remaining nonbonding terms are Lennard-Jones interactions (using the Lorentz-Berthelot mixing rule[18] to obtain the LJ parameters; i.e. the usual LJ potential parameters ϵ_{ij} and σ_{ij} are expressed as $\epsilon_{ij} = \sqrt{\epsilon_i \epsilon_j}$ and $\sigma_{ij} = \sigma_i + \sigma_j$, where the indices label the interacting atoms and a factor 0.5 has been absorbed into σ_i and σ_j), Coulomb interactions, and hydrogen bond interactions. Note that all LJ and Coulomb 1-4 nonbonded interactions (nonbonded atoms separated by three bonds) are scaled by a factor 0.5.[20] As far as the potential parameters are provided, they are adopted from the AMBER data base.[20] Valence and dihedral potential parameters, which are not contained in the data base, are calculated using the MNDO (modified neglect of diatomic overlap) method (cf. Table 1). The atomic partial charges are calculated for the "all-atom" case using the charge equilibration method[22] as provided in the software package POLYGRAF.[23] We make the transition to the united atom model by adding the charges obtained for the hydrogens to the charge of the respective carbon atoms. For DMF we can compare the result of the so obtained (united atom) dipole moment of $\mu = 3.27$ D to the experimental value of $\mu_{exp} = 3.24$ D.[19] Interestingly, in ref 24 an ab initio quantum mechanical calculation yields $\mu = 4.34$ D and thus less good agreement. The entire parameter set used here is compiled in Table 1.

Before starting the actual simulation we energy-minimize the initial configuration in order to relax possible van der Waals overlaps. Note that during the energy minimization as well as during the subsequent MD simulation all nonbonded interactions are omitted beyond a residue based cutoff of 10 Å, where the residues are the PBLG repeat units and the solvent molecules, respectively. Thus if at least two atoms belonging to different residues are separated by less than 10 Å, the nonbonded interactions are calculated between all atoms belonging to the two residues. During the MD simulation the atomic equations of motion are solved using a leap-frog version of the Verlet-Störmer algorithm with a 2-fs time step, keeping the bond lengths fixed using the SHAKE algorithm.[25] Note in this context that especially for protein molecules van Gunsteren and Karplus[26] have shown that the fixing of high bond length oscillations by introducing adequate constraints has little effect on the structure and the dynamics. Throughout the initial thermalization and equilibration process we employ *NVT* dynamics at 300 K (particle number, volume, and temperature are kept constant) using velocity scaling according to ref 27 to obtain the desired temperature. The preequilibrated system is then entered into a *NVE*-MD run (particle number, volume, and total energy are kept constant) without velocity scaling. The first 150 ps of the simulation are discarded from the analysis as the time necessary for equilibration.

The simulation consists of two separate runs. During the first run we concentrate on the dynamics of the PBLG side chain–DMF interface, where the PBLG backbone atoms are kept fixed by introducing mechanical constraints. This simulation is characterized by an average temperature of 313 K. Over a simulation length of 850 ps the standard deviation of the total energy is less than 0.35%. During the second run, the backbone is allowed to move freely in the solvent matrix. Here, we obtain an average temperature of about 298 K over a simulation time of 700 ps. The stability of the system is characterized by an energy standard deviation less than 0.46%.

Fixed Backbone Simulations

The results in this section are based on a simulation during which the atoms of the helix backbone were not allowed to move. Only the side chain atoms as well as the solvent atoms retain their full dynamical freedom, because here we are interested solely in the structure and dynamics of the side chain–solvent interface. The reanalysis of the results presented here based on the unconstraint simulations discussed in section II does not yield significant differences due to the local rigidity of the backbone. However, the precise definition of proper reference frames along the moving backbone introduces unnecessary difficulties and reduces the transparency of the presentation significantly.

(a) Characterization of the Solvent–Side Chain Interface. Radial Density and Order Parameter Profiles. Figure 2A shows the center of mass number density ρ of DMF as a function of the distance r from the axis of the PBLG helix. More precisely, r is the distance between the center of the C–N bond and the center of mass of the PBLG backbone. Note also that the density is normalized to the experimental bulk density ρ_{bulk} at $T = 300$ K for large r. The peaks in the distribution correspond to locally preferred radial positions of the DMF molecules with respect to the PBLG helix. The range of the structured region, i.e. the solvation zone, extends out to a distance of approximately 15 Å from the helix axis. For comparison, Figure 2A also shows the radial extension of the PBLG side chains based on the center of mass distribution of the phenyl rings again in terms of the distance r from the helix axis. Notice that the phenyl center of mass distribution ranges from ~5 to ~10 Å and exhibits two pronounced peaks at ~6 and ~9 Å (as an aside, we mention that an analogous simulation of PBLG in vacuum only yields the side chain peak at ~6 Å).

Because phenyl rings are quite large it is useful to also consider their average orientation, i.e. whether they are "pointing away" from the helix axis (as suggested in the insert of panel B) or whether they are "pointing along" the helix axis. This information is contained in the insert in Figure 2A, which shows the phenyl center of mass distribution overlayed with the distribution of the phenyl C atom, which has the largest distance from the helix if the side chain is fully extended (indicated by an X in the sketch). For large r, the offset between the two distributions is close to 1.4 Å, i.e. the distance between the phenyl carbons and the phenyl center of mass, which indicates that the phenyl rings are preferentially pointing away from the helix. With decreasing r the offset also decreases slightly, and for $r < 5$ Å, there is no offset, which indicates that the phenyl axis defined by cm and X is parallel to the helix. In particular, the phenyl distributions also show that the helix induced liquid structure extends beyond the range of the side chains. In this context it is worth noting that the analysis of simultaneous static and dynamic light scattering measurement strongly suggests that the effective diameter of PBLG in DMF is close to 30 Å.[13] This diameter is in excellent accord with the range of the solvation shell structure in the DMF density distribution shown in Figure 2A, provided one considers the DMF layer corresponding to the peak at ~15 Å, which lies beyond the intermediate range of the side chains, as an integral part of the helix in solution. As we show below, this notion is also supported by the fact that solvent molecules within this region are distinguished by a lower mobility in comparison to the bulk fluid and thus "stick" to the helix.

In addition to the DMF center of mass density profile, Figure 2B shows the radial dependence of the orientation order parameter

$$S_\theta = \frac{3\langle \cos^2 \theta \rangle - 1}{2} \tag{3}$$

where θ is the angle between the helix axis and the surface normal of the DMF molecular plane, and r is again the distance between the center of the C–N bond and the helix axis. The surface normal of the DMF molecular plane is defined by the cross product of the two unit vectors along the C–N and C–O bond (cf. the insert in Figure 2B).

Table 1. Force Field Parameters and Partial Charges for PBLG and DMF[a]

bonds	f_r (kcal mol^{-1} Å^{-2})	r_{equ} (Å)	ref	bonds	f_r (kcal mol^{-1} Å^{-2})	r_{equ} (Å)	ref
H-N	SHAKE	1.01		C-N	SHAKE	1.34	
C-C2	SHAKE	1.52		CH-C2	SHAKE	1.53	
C-CH	SHAKE	1.52		C2-C2	SHAKE	1.53	
C-O	SHAKE	1.23		C2-OS	SHAKE	1.42	
C-OS	SHAKE	1.36	21	N-C3	SHAKE	1.45	
CA-CD	SHAKE	1.40		CH-O	SHAKE	1.42	:=CH-OS
CA-C2	SHAKE	1.51		CH-N	SHAKE	1.47	
CD-CD	SHAKE	1.40		N-C3	SHAKE	1.45	

angles	f_δ (kcal mol^{-1})	δ_{equ}	ref	angles	f_δ (kcal mol^{-1})	δ_{equ}	ref
N-CH-C2	80	109.7		CD-CA-C2	70	120.0	
C-CH-N	63	110.1		CA-CD-CD	85	120.0	
CH-N-H	38	118.4		CD-CD-CD	85	120.0	
CH-C2-C2	63	112.4		CD-CA-CD	85	120.0	
CH-C-O	80	120.4		CH-C-N	70	116.6	
C-C2-C2	63	112.4		N-C-O	80	122.9	
C-CH-C2	63	111.1		C-N-H	35	119.8	
C2-C-O	80	120.4		C-N-CH	50	121.9	
C2-C-OS	81	111.4		CH-N-C3	50	121.9	:=C-N-C3
C-OS-C2	90	126.7	MNDO	O-CH-N	80	122.9	:=N-C-O
O-C-OS	80	126.0	21	C3-N-C3	50	121.9	:=C-N-C3
OS-C2-CA	142	109.1	MNDO				

dihedral angles	f_n (kcal mol^{-1})	γ	n	ref	dihedral angles	f_n (kcal mol^{-1})	γ	n	ref
X-CH-C2-X	2.0	0	3		X-C2-OS-X	1.45	0	3	
O-C-CH-N	0.1	180	3		X-CA-C2-X	0.0	0	2	
X-CH-N-X	6.2	180	2	MNDO	X-CA-CD-X	5.3	180	2	
X-C2-C2-X	2.0	0	3		X-CD-CD-X	5.3	180	2	
X-C2-C-X	0.0	180	3		X-C-CH-X	0.0	0	2	
O-C-CH-C2	0.1	180	3		X-C-N-X	10.0	180	2	
X-C-OS-X	10.0	180	2	21	X-CH*-N-X	6.2	180	2	MNDO

LJ Parameters

	ϵ (kcal mol^{-1})	σ (Å)		ϵ (kcal mol^{-1})	σ (Å)
H	0.02	1.00	C3	0.15	2.00
OS	0.15	1.65	C	0.12	1.85
O	0.20	1.60	CD	0.12	1.85
CH	0.09	1.85	N	0.16	1.75
C2	0.12	1.925			

Partial Charges

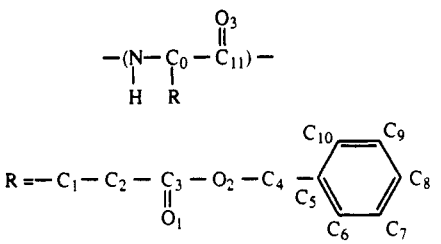

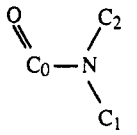

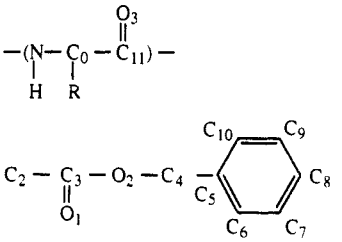

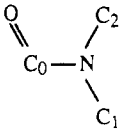

PBLG	q (electron charges)	DMF	q (electron charges)	PBLG	q (electron charges)	DMF	q (electron charges)
N	-0.498	C_0	0.51	C_5	0.082		
H	0.309	O	-0.48	C_6	0.019		
C_0	0.177	N	-0.39	C_7	0.011		
C_1	0.067	C_1	0.12	C_8	0.015		
C_2	0.007	C_2	0.24	C_9	-0.004		
C_3	0.613			C_{10}	0.081		
O_1	-0.475			C_{11}	0.514		
O_2	-0.536			O_3	-0.575		
C_4	0.193						

[a] The force field parameters are extracted from the AMBER data base,[20] as far as they are provided. Parameters not contained in the AMBER parameter list are referenced separately. We use the AMBER atom type convention: H = amide hydrogens, N = nitrogen in amide groups, O = carbonyl oxygen, OS = ether and ester oxygens, C = carbonyl carbon, CH = carbon with one hydrogen, C2 = carbon with two hydrogens, C3 = carbon with three hydrogens, CD = aromatic carbon in six-membered ring with one hydrogen, CA = aromatic carbon in six-membered ring with one substituent. The partial charges are calculated via the charge equilibration algorithm,[22] which is part of the POLYGRAF[23] modeling package.

If the DMF surface normal is oriented parallel to the PBLG axis $S_\theta = 1.0$, whereas for perpendicular orientation $S_\theta = -0.5$. Figure 2B shows that the modulation of the order parameter profile closely follows the shell structure shown in panel A, where the surface normal of the DMF molecules in the immediate vicinity of the helix is strongly tilted away from the helix axis. Notice that the DMF molecules change the preferential orientation of their molecular plane within the first solvation shell; i.e. the order parameter minimum at 5.2 Å indicates a tilt of the DMF surface

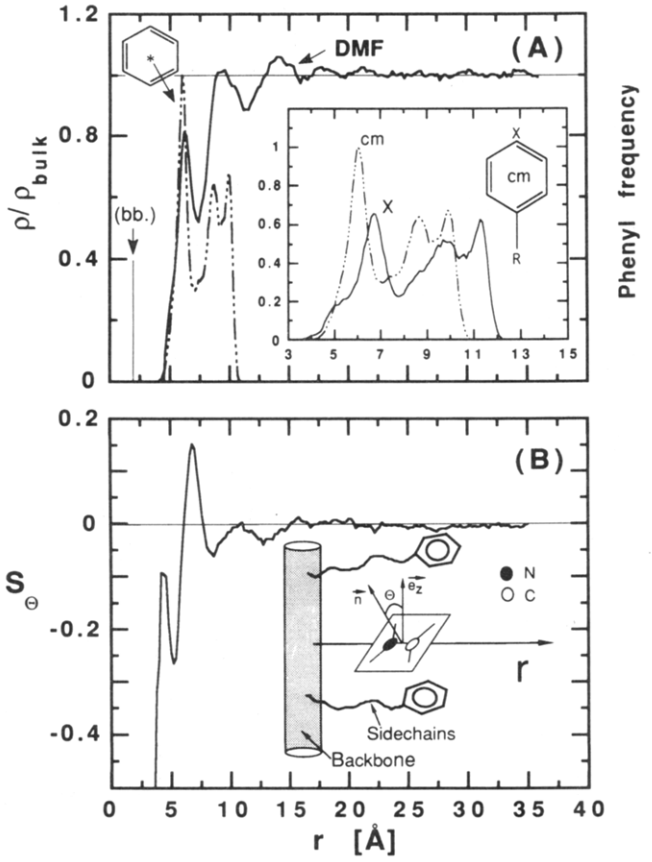

Figure 2. (A) Solvent density ρ divided by the bulk density ρ_{bulk} as a function of distance r from the helix axis (full curve) and radial center of mass distribution of the PBLG phenyl rings (dashed-dotted curve). Note that (bb.) denotes the radial position of the α-carbons. The insert shows an expanded view of the radial center of mass distribution of the phenyl rings (cm) and, in addition, the radial distribution of the phenyl carbon denoted by X in the included sketch. (B) Radial dependence of the orientational order parameter S_Θ. Here Θ is the angle between the axis perpendicular to the molecular plane of the DMF molecules (defined via the bond vectors C–N and C–O and the helix axis) as indicated in the sketch.

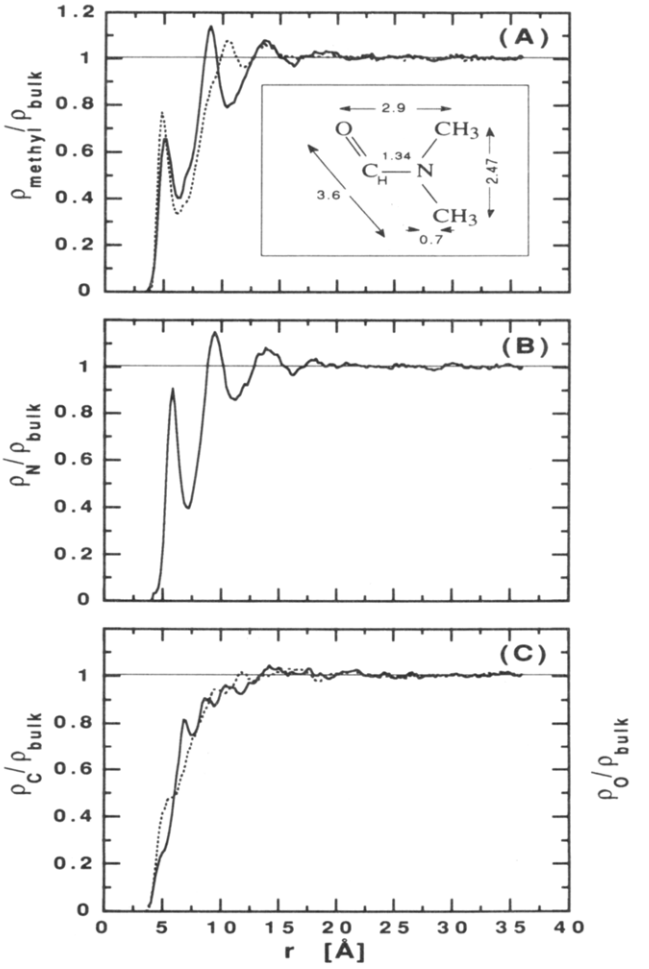

Figure 3. DMF atomic density profiles. (A) Methyl carbons in cis (solid line) and trans (dotted line) position relative to the oxygen, (B) nitrogen, and (C) carbonyl carbon (solid line) and oxygen (dotted line) as a function of distance r from the helix axis. The sketch in panel A illustrates various equilibrium interatomic distances in the DMF molecule.

normal away from the helix axis, whereas the subsequent maximum at 6.8 Å indicates a small preferential tilt of the surface normal toward the helix axis.

Figure 3 analyzes the induced solvent structure in more detail, showing the atomic radial density distributions for the two methyl groups (A), for the nitrogen (B), and for both carbonyl atoms (C). As before, all curves are normalized to the bulk density of DMF. Notice that the shell structure appears much more pronounced in the methyl and nitrogen distributions than in the carbonyl distributions, i.e. it is the bulkiness of the $N(CH_3)_2$ group rather than the polar character of the carbonyl group which governs the solvation shell structure. Notice also that in the first shell, the methyl groups are preferentially oriented toward the helix and that the two methyl peaks at 4.8 and 5.0 Å closely coincide. The corresponding nitrogen peak is at 5.7 Å, indicating a strong tilt of the N–C bond away from the helix. This is because the projection of the N–(CH_3) bonds onto the C–N axis is about 0.7 Å (cf. the insert in Figure 3A), which closely corresponds to the separation between the methyl peaks and the nitrogen peaks. Interestingly, in the second shell, the methyl peaks are separated by 1 Å, bracketing the corresponding nitrogen peak, so that the cis-methyl group (defined with respect to the oxygen) and therefore the carbonyl group is now rotated toward the helix.

(b) Characterization of the Solvent–Side Chain Interface. Azimuthal Structure. Here we calculate the atomic pair correlation functions

$$g_{ij}(r,r') = \langle \rho_i^*(r,0)\rho_j^*(r,r') \rangle \quad (4)$$

which give the probability of finding two atoms of type i and j separated by a distance r' within a cylindrical shell of radius r (measured between the helix axis and the middle of the shell) and width $\Delta r = 0.5$ Å. Notice that $\rho^* = \rho/\rho_{bulk}$. The separation r' along the cylinder surface is given by $r' = \sqrt{z^2 + (\varphi r)^2}$, where z is the separation of the atom pair parallel to the cylinder axis and φ is the angular separation of the atom pair in the plane of the cylinder cross section. Notice also that the periodic image convention is applied.

The resulting pair correlation functions g_{CC}, g_{NN}, and g_{CN} for DMF are shown in Figure 4A–C. The correlation functions are calculated for two different radii r in order to compare the bulklike region (r = 32 Å) with the immediate vicinity of the helix (r = 5.95 Å). The solvent pair correlation functions for r = 32 Å show the liquidlike order in the peripheral region of the simulation box. The first maxima at 5.4, 4.7, and 4.0 Å of the N–N, N–C, and C–C correlation functions correspond to the nearest neighbor separations for these atom pairs; i.e. they basically reflect the closeness of the carbonyl group compared to the larger separation of the bulky N–(CH_3)$_2$ groups. Notice that the polar character of the carbonyl group manifests

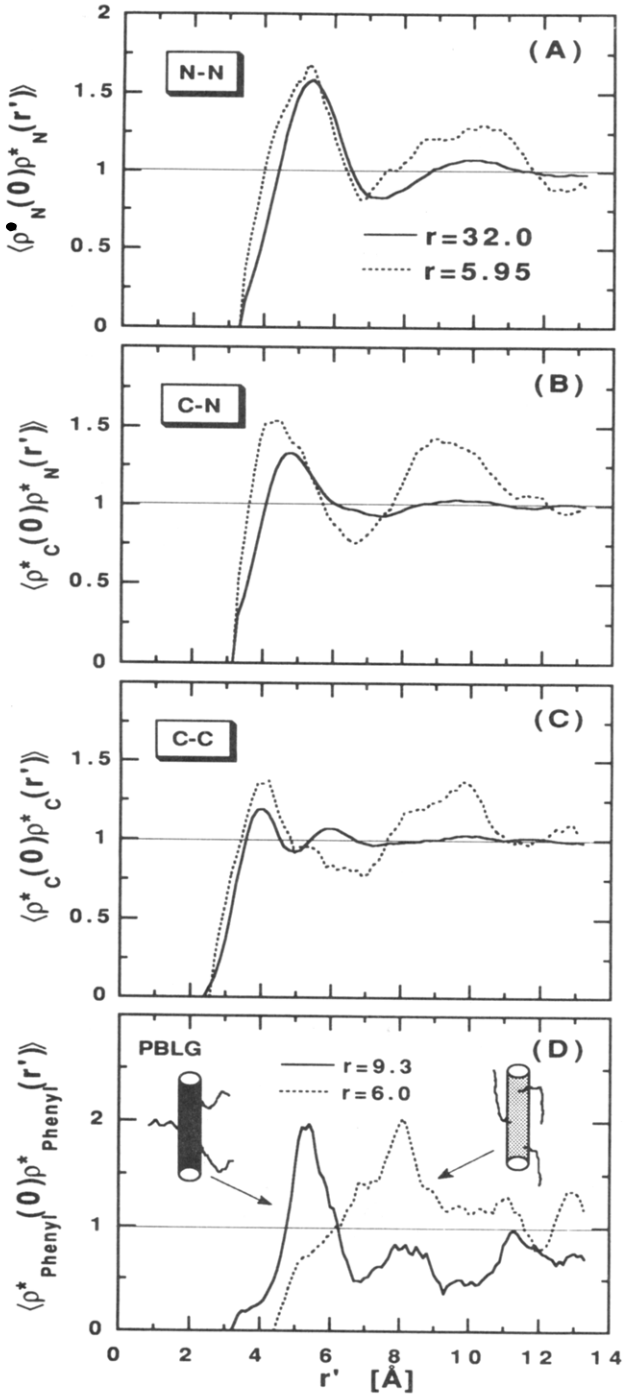

Figure 4. DMF atomic pair correlations within cylindrical shells of radius r and width Δr centered on the helix axis: (A) nitrogen–nitrogen, (B) carbon–nitrogen, (C) carbon–carbon correlation function. The two shell radii are r = 32 Å (solid line) and r = 5.95 Å (dotted line), and r' is the interatomic separation along the cylinder surface. (D) Corresponding center of mass pair correlation function for the PBLG phenyl rings for r = 9.3 Å (solid curve) and r = 6.0 Å (dotted curve).

itself in a differentiation of the first neighbor shell into two separate peaks. Beyond the first neighbor shell, the bulk correlations are strongly diminished. In comparison, the surface correlations within the cylindrical shell at r = 5.95 Å exhibit very similar nearest neighbor correlations. However, the second neighbor peaks are much more pronounced due to the ordering induced by the helix surface.

Panel D in Figure 4 shows the pair correlation functions for the side chain phenyl rings, where r' is now the separation between the phenyl centers of mass. The two curves compare the pair correlations between the side chains calculated within cylindrical shells bracketing the peaks in the phenyl center of mass distribution shown in Figure 2A. Unfortunately, the statistics is not so good in this case. However, on average, the nearest neighbor separation of the phenyl rings corresponding to the density peak at r = 6.2 Å is significantly increased in comparison to the nearest neighbor separation of the phenyl rings corresponding to the density peak at r = 9.6 Å. This is consistent with the picture that for small axial separations the side chains possess more angular freedom orienting themselves in different directions along the helix surface but show no tendency to pair up. At larger axial separation, however, the side chains are stretched, and the peak at r' = 5.3 Å corresponds closely to the inter-phenyl distance for regularly arranged stretched side chains, as shown in the upper portion of Figure 2.

(c) Solvent Bulk and Surface Diffusion. Throughout this work the DMF molecules are described in terms of the united atom model, which means that CH, CH_2, and CH_3 groups are treated as effective single atoms with different van der Waals radii. One good check of the quality of this approximation is to compare the simulated bulk self-diffusion coefficient to the experimental bulk self-diffusion coefficient, because it is rather sensitive to the molecular excluded volume. Here we calculate the bulk diffusion coefficient D via the Einstein relation

$$D = \lim_{t\to\infty} \frac{1}{6t} \langle \Delta \vec{r}_i^{\,2} \rangle_{i,t_0} \tag{5}$$

as well as the in-plane diffusion coefficients D_{xy}, D_{xz}, and D_{yz} defined by

$$D_{\alpha\beta} = \lim_{t\to\infty} \frac{1}{4t} \langle (\Delta \vec{r}_i)_{\alpha\beta}^{\,2} \rangle_{i,t_0} \quad \text{with} \quad \alpha\beta = xy, xz, yz \tag{6}$$

where $\Delta\vec{r}_i$ is the displacement of solvent molecule i during the time interval t and $(\Delta\vec{r}_i)_{\alpha\beta}$ is the projection of $\Delta\vec{r}_i$ onto the $\alpha\beta$ plane. To calculate the diffusion coefficients we concentrate on solvent molecules initially contained in a thin slab of thickness d = 5 Å at the simulation box boundary. Based on the trajectories of the molecules i, which are initially in the slap, we calculate the quadratic displacement $\Delta\vec{r}_i^{\,2}(t)$ and the projections $(\Delta\vec{r}_i(t))_{\alpha\beta}^{\,2}$ for a given displacement time t. These quantities are then averaged over the molecules i as well as with respect to different time origins t_0 separated by 0.1 ps along the simulation trajectory. Figure 5 shows the mean square displacement (divided by 6) as well as the mean square of the projections (divided by 4) onto the xy-, xz-, and yz-planes as a function of the displacment time t. Note that up to 120 ps the mean square displacements differ only slightly, which indicates bulklike isotropic motion of the solvent molecules; i.e. no direction is preferred. After approximately 130 ps the diffusion deviates from the isotropic behavior. This time it corresponds to $\langle \Delta\vec{r}^{\,2} \rangle^{1/2} \sim 14$ Å; i.e. the molecules, which are initially at the periphery of the simulation box, begin to interact with the solvation shell of the PBLG helix (cf. Figure 2A). Note that the diffusion in the xy-plane toward the PBLG molecule (xy-plane) is clearly smaller than the diffusion parallel to the helix axis (xz- and yz-planes). At root mean square separations less than 12 Å from the helical backbone (t > 250 ps) the overall mobility decreases again. To calculate the self-diffusion of DMF in the bulk we concentrate on the molecular displacements during the first 80 ps. The diffusion coefficient is calculated from the slope of a linear fit to the data shown in the insert of Figure 5. We obtain $D = 2.2 \times 10^{-9}$ m^2/s at T = 313 K,

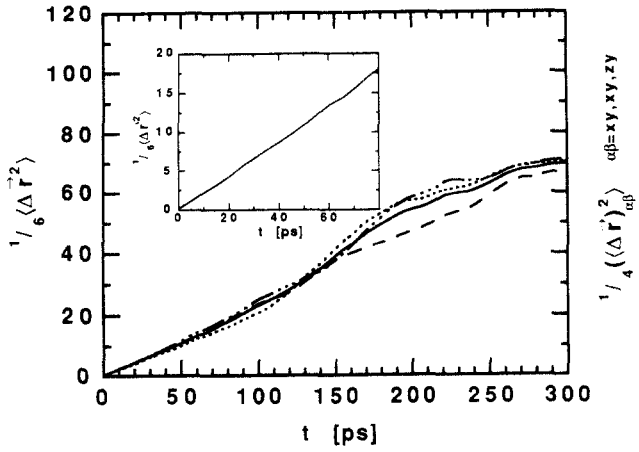

Figure 5. Mean square displacement divided by 6 vs time t (solid line). Mean square displacement in the xy-plane (dashed line), and in the xz-plane (dashed dotted line), and in the yz-plane (dotted line) divided by 4 vs time t. The insert shows the mean square displacement divided by 6 during the first 80 ps. A linear fit yields the bulk diffusion coefficient $D = 2.2 \times 10^{-9}$ m^2/s. Note that the mean square displacements are calculated for molecules initially at the periphery of the simulation box.

which has to be compared to the experimental value of 1.98×10^{-9} m^2/s.[28] The quite reasonable agreement of the calculated bulk diffusion with the experimental result indicates that the united atom model used in this simulation appears to provide a satisfactory description for DMF.

In addition to the bulk diffusion, it is interesting to study the exchange of solvent molecules between different solvation shells as well as between the solvation zone and the bulk. More precisely, we study the time evolution of solvent density profiles for molecules whose center of mass initially (t = 0) is within a cylindrical shell around the helix axis of radius r and thickness Δr = 3 Å. As above, we shift the time origin over the simulation trajectory in steps of 0.1 ps and average over the profiles corresponding to the different time origins. Figure 6 shows the time evolution of the solvent density profiles for molecules whose center of mass initially is in the range between 8 and 11 Å (A), 13 and 16 Å (B), and 20 and 23 Å (C). The initial density distributions are segments of the DMF density distribution shown in Figure 2A, where (A) and (B) bracket the second and third density peak, and (C) is a segment in the bulk. Note that for reasons of scale, the maximum of the initial contributions is cut off in Figure 6. The profiles at later times are averages calculated over the time intervals Δt = 50, 100, and 150 ps.

Figure 6A shows the time evolution of the position of the solvent molecules in the brushlike region consisting of side chains and solvent molecules. After 50 ps the density in the original segment has decreased to roughly half its initial value, and the molecules are now significantly accumulated in the adjacent solvation shells. Notice that even after 150 ps the surface induced shell structure is still discernible. A similar but less pronounced behavior is shown in Figure 6B, where the molecules are initially at the periphery of the solvation shell. Finally, in comparison, Figure 6C illustrates the short time diffusion of the solvent molecules in the bulk. Note that in this case, after 150 ps the molecules are spread quite evenly over the entire width of the simulation box. The fact, that solvent molecules which are initially in the solvation zone remain localized significantly longer than if they are initially in the bulk, indicates that one has to consider the structured solvent shell as an integral part of the PBLG molecule. However, the time development of the above

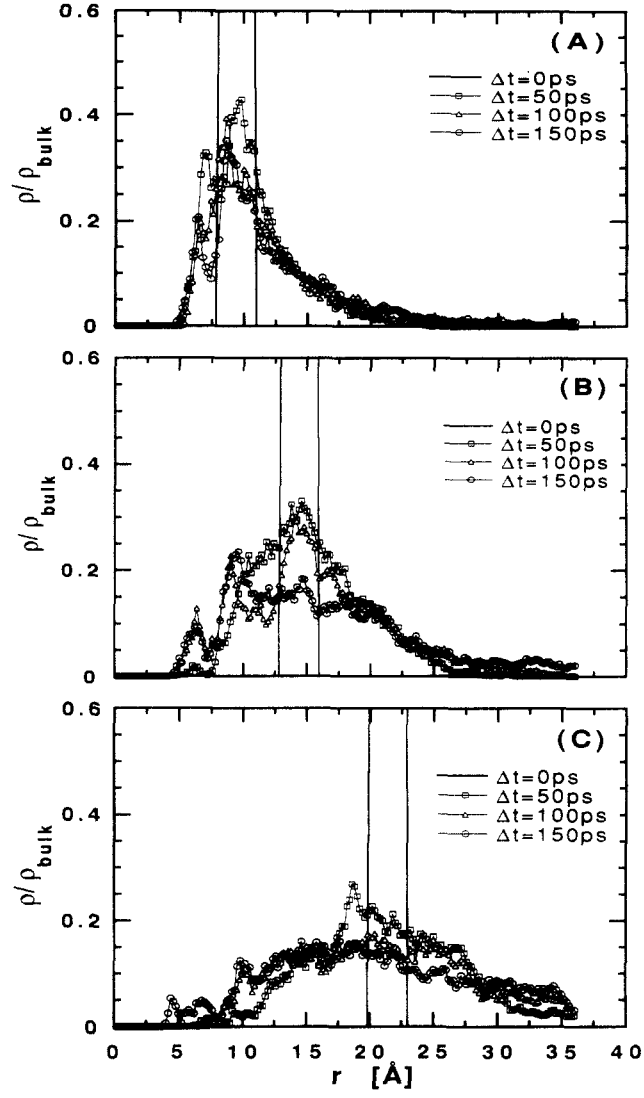

Figure 6. Time evolution of three different radial segments in the DMF center of mass density profile shown in Figure 2A. The molecules are initially ($t = t_0$) contained in the radial intervals 8–11 Å (A), 13–16 Å (B), 20–23 Å (C) indicated by the vertical lines. With time, the molecules spread throughout the system. The curves are average radial distributions of the initially localized molecules based on the time slices $t = t_0 + 0$ ps (–), $t_0 + 50$ ps (□), $t_0 + 100$ ps (△), and $t_0 + 150$ ps (○).

density profiles also shows that there is a significant exchange of solvent between the solvation shell and the bulk during the simulation time of 850 ps, which is necessary to establish equilibrium between the different parts of the system.

Free Backbone Simulations

The results presented in this section are for the freely moving helical backbone without mechanical constraints, where now the main focus is on the longitudinal and transverse elastic properties of the helix itself.

(a) Hydrogen Bond Length and Angular Distributions. The PBLG α-helix is stabilized by the formation of C=O···H—N hydrogen bonds. More precisely, the C=O···H—N hydrogen bonds are formed between the C=O group of the nth peptide unit and the N—H group of the $(n + 4)$th peptide along the polypeptide chain. The hydrogen bonds are found to be nearly parallel to the helix axis, and the C=O groups are slightly tilted and displaced away from the helix axis.[15] A useful characterization of the hydrogen bonds along the PBLG backbone can be given in terms of the N···O distance and the HN···O angle.

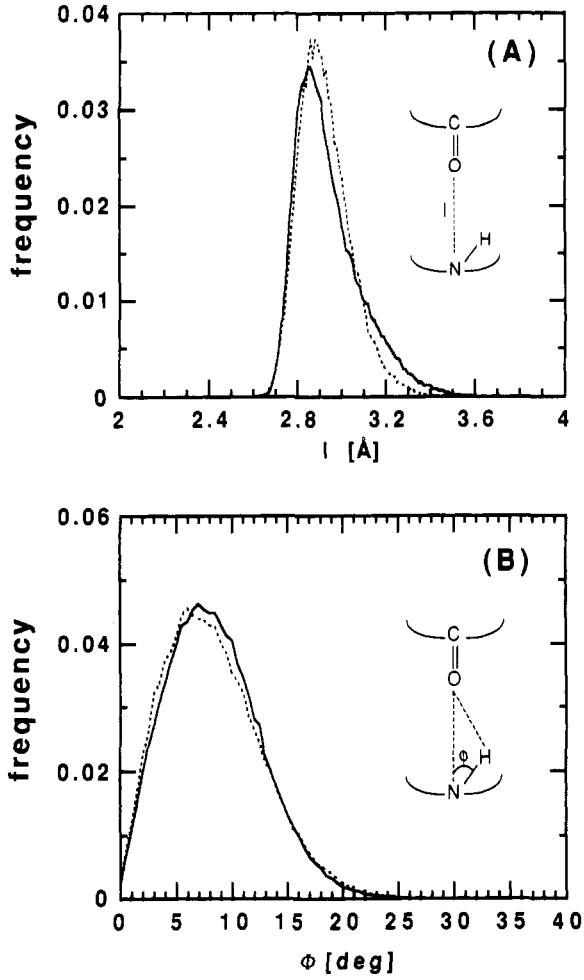

Figure 7. Internal hydrogen bonds of PBLG in DMF (solid line) and in vacuum (dotted line). (A) Distribution of the N···O distance l. (B) Distribution of the angle ϕ between HN···O. The sketches in panels A and B illustrate the geometry of the bonds.

On the basis of energy minimizations for α-helices, Donohue[29] obtains for the N···O distance 2.86 Å and for the HN···O angle a value of 4° in the crystalline state.

In order to estimate the effect of solvent on the hydrogen bond stabilization of the helical backbone, we have extracted both the N···O distance and the HN···O angle from the simulation. Part A and B of Figure 7 show the distribution of the N···O distance and HN···O angle obtained from the trajectories of the PBLG/DMF and an analogous PBLG/vacuum simulation. In the presence of DMF, the distribution function of the hydrogen bond distance attains its maximum at a distance, which coincides with the value calculated by Donohue. The maximum of the HN···O angle distribution, however, is different from the suggested value and reaches its maximum at 7°, while the width at half-maximum is about 11°. Interestingly, the differences between the DMF and the vacuum results are rather minor; i.e. the bond length distribution is slightly broadened in DMF.

A detailed analysis of the backbone motion shows that the helix undergoes both torsional motions—that is twisting and untwisting of the helix—and slight bending motions in the z-direction. Although the dynamic of the helix is influenced by its torsional motion, the shape of the N···O separation profile is determined by the bending motion of the helix. In the case of the helix in a vacuum the bending motion has a slightly smaller effect on the N···O separation, resulting in a slightly sharper distribution of the N···O distance.

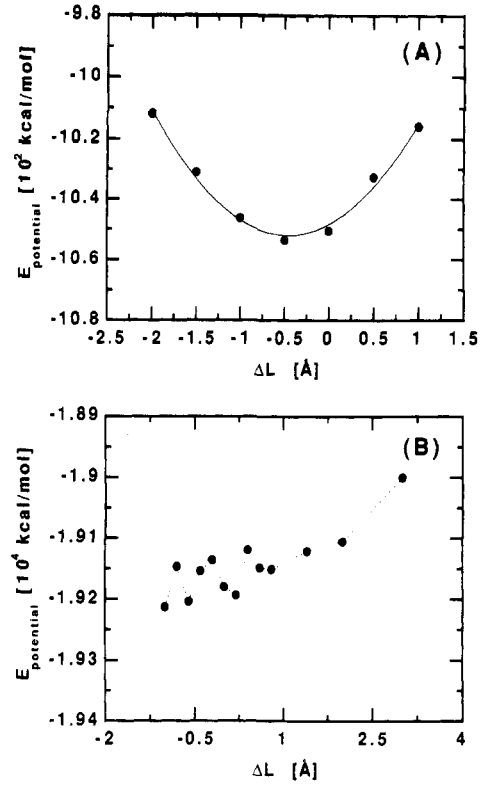

Figure 8. Total potential energy of (A) PBLG in a vacuum and (B) PBLG in DMF as a function of the strain ΔL of the helix axis in z-direction.

(b) Helix Response to Limited Tension and Compression. In order to obtain information about the elastic properties of PBLG we study the response of the helix to static tensile and compressive strain. Assuming perfect elasticity we can make use of Hooke's law

$$\sigma = E\epsilon \tag{7}$$

where σ and ϵ represent the tensile stress and strain, respectively, and E is the axial Young modulus. In order to obtain E we can write $\sigma = F/A$ and $\epsilon = \Delta L/L$, where F denotes the normal force acting on the effective elastic cross section A of the polymer, ΔL is the elongation of the molecule axis in z-direction, and $L = 27.04$ Å is the initial length of the helix axis. To calculate the force F, we fit the total energy of the system obtained through energy minimizations to a harmonic potential

$$V = \frac{1}{2}k\Delta L^2 \tag{8}$$

where the force constant k is a fit parameter. Thus F is given by $F = k\Delta L$ and therefore

$$E = kL/A \tag{9}$$

To simulate a stepwise compression/tension of the PBLG molecule we reduce/increase the molecular extension in the z-direction by ΔL at each step by changing the z-coordinates of the PBLG atoms homogeneously. After each instantaneous step we carry out a short NVT molecular dynamics simulation at 300 K followed by an energy minimization.

First we study the response of the helix in a vacuum where we change the molecular extension by 0.5 Å per step and perform a 5-ps MD run following each step. The resulting total potential energy thus obtained is shown in Figure 8A as a function of ΔL. From the potential fit included in Figure 8A we obtain the force constant $k = 34$ kcal/(mol Å^2). To obtain an estimate of the cross section A of PBLG in the bulk we consider the cross sectional

area per helix of parallel packed PBLG molecules in the solid phase. On the basis of the solid density ρ_{PBLG} = 1.3 g cm^{-3} [30] we obtain an effective helix radius of 7.7 Å. Note that this value is in close accord with the minimum between the two peaks in the phenyl distribution shown in Figure 2A. Thus, for Young's modulus we obtain 34 GPa.

Dynamic measurements on PBLG films made with a free oscillating torsional pendulum show a strong temperature dependence of the dynamic shear modulus.[31] Especially at $T > 260$ K a sharp drop of the shear modulus is observed, which is attributed to a relaxation process due to side chain motion. Jackson et al.[30] calculate the dynamic tension modulus E based on the shear modulus data of ref 31 as a function of temperature and obtain tension moduli between E = 3.1 GPa (T = 286 K) and E = 0.78 GPa (T = 301 K). We see three main reasons for the significant gap between the low-temperature experimental value and the zero-temperature result of the static energy minimization. First, there is the unknown experimental error composed of the error for the estimated Poission's ratio as well as the experimental error for the shear modulus. Second, the simulation result is for a single chain, whereas the experimental result is obtained on a bulk sample. Finally, there is the above-mentioned neglect of entropic contributions in the static energy minimization.

Figure 8B shows the corresponding strain–energy relation for PBLG in DMF over a range of axial strains. Here we change the z-dimension of the simulation box by only 0.2 Å per step, in order to obtain fast relaxation of the solvent structure. The other box dimensions change accordingly to preserve the box volume. Each rescaling of the PBLG segment is followed by a 2-ps NVT MD run. The potential energy is now of course very different from the vacuum case due to the additional interactions of PBLG with the surrounding solvent as well as due to the bulk interactions of the solvent, which are difficult to subtract due to the complex structure of the interface. However, even though there is considerable scatter, Figure 8B shows that the helix resists tensile strain, which is consistent with the above mentioned indirect conclusions[9,13] that PBLG preserves its conformation upon dilution in DMF.

(c) Simulation of the Persistence Length. Molecular flexibility strongly affects the mechanical and thermodynamic behavior of a polymer system. The experimental determination of the flexibility of a given polymer, however, is often plagued by various difficulties. For instance, sample polydispersity or the model dependence of the data analysis may lead to considerable scatter of the reported results obtained on the same system.[13] It is therefore interesting to apply atomistic computer simulation techniques to this question, which allow well defined realistic conditions avoiding the above difficulties.

In the context of flexibility PBLG is best described as being persistent flexible or homogeneously bend-elastic. The measure of this type of flexibility is the persistence length P defined by

$$\langle \vec{u}(0)\vec{u}(s) \rangle = e^{-s/P} \tag{10}$$

where the left hand side of eq 10 denotes the orientation correlation function between two unit vectors tangential to the molecular contour, which are separated by a distance s[32] (cf. Figure 9). Thus, only on a length scale $\ll P$ can the molecule be considered rigid, whereas on a length scale $\gg P$ it is best described as being wormlike flexible. Because P may vary depending on the type of solvent (cf. ref 7 and references therein), it is desirable to explicitly include the solvent if one wants to determine P via a computer simulation. However, for large P (for PBLG in DMF the experimental values range from 700 to 1400 Å[13]) an appropriate simulation box containing both polymer and solvent with dimensions at least equal to or exceeding the expected persistence length still requires a prohibitively large computational effort. However, it is not P directly, which determines the size of the simulation box, but rather the spatial range along the polymer contour over which flucutations of the internal coordinates, i.e. bond length, valence, and dihedral angles, are correlated. Often it turns out to be sufficient to simulate a polymer segment much shorter than the persistence length and estimate P on the basis of the valence angle and dihedral statistics of this segment. In the following, we analyze the simulation trajectory of the unconstrained backbone on the basis of this assumption by employing an approach which involves

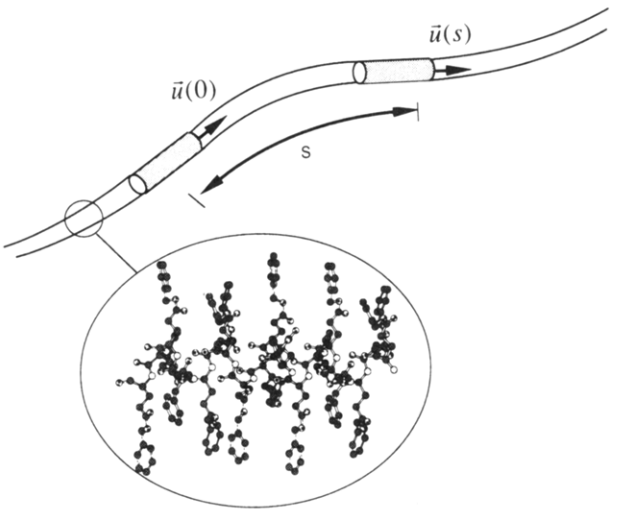

Figure 9. Schematic illustration of a PBLG molecule as a persistent flexible rod. Short sections of the PBLG backbone can be approximated by cylinders, whose axes allow one to define vectors $\vec{u}(0)$ and $\vec{u}(s)$, which are tangential to the molecular contour at the positions 0 and s.

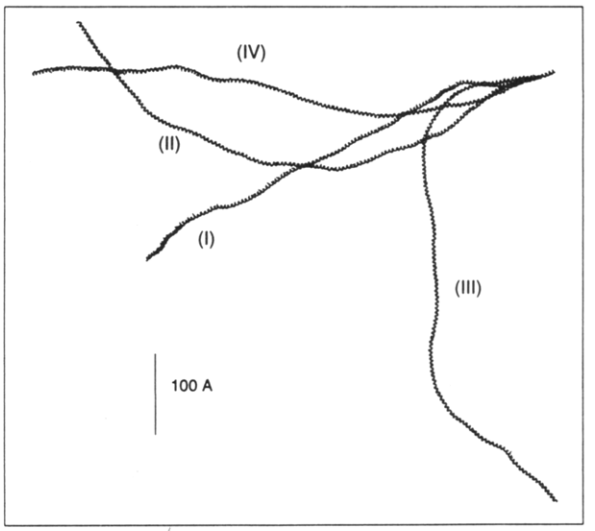

Figure 10. Subsections of the high molecular weight PBLG fragments constructed according to the procedure explained in the text. The fragments shown in the figure are based on the PBLG/DMF simulation and correspond to different time intervals Δt at which a backbone conformation is extracted from the trajectory: (I) Δt = 0.5 ps (8657 monomers) (II) Δt = 1.0 ps (4329 monomers), (III) Δt = 1.5 ps (2882 monomers), (I V) Δt = 2.0 ps (2161 monomers). Only 500 monomers of each constructed helix are shown.

the direct application of eq 10. Note that the complex structure of PBLG makes it rather difficult to apply transfer matrix methods as are commonly used for simpler polymer structures.[33]

A reliable calculation of the persistence length from eq 10 requires contour lengths close to or preferably exceeding the (expected) persistence length. Here we construct such high molecular weight fragments of the PBLG backbone by connecting instantaneous conformations of the short simulated segment under the "smoothness" condition that the local conformation of the "tail" of segment n has to match the local conformation of the "head" of segment $n + 1$.

More precisely the procedure is as follows. First we extract the conformations of the unconstrained PBLG backbone segment from the above simulation at regular time intervals Δt. The bond lengths are kept fixed during the simulation and thus a specific conformation corresponds to a certain sequence of valence and dihedral angles. Because in the present case the fluctuations of the valence angles around their equilibrium values are small, we replace the different valence angles by their simulation averages. Thus, what we finally extract from the simulation trajectory are the backbone dihedral angles of the simulated PBLG segment. Even though this segment consists of 18 monomers, we only use the dihedral angles of 9 successive monomers in order to avoid boundary effects. On the basis of the extracted 9-mer dihedral angles, in a second step, we build a high molecular weight fraction of the PBLG backbone. Let us assume that such a fragment consisting of n 9-mers already exists. The above list of 9-mers is then searched for the 9-mer whose first dihedral angle is closest to the last dihedral angle of the nth 9-mer in the high molecular weight fragment. Discarding this overlapping dihedral angle the selected 9-mer becomes the $n + 1$ unit of the backbone fragment. At the same time, the added 9-mer is deleted from the list of conformations, and the second step in the above procedure is repeated. The result is shown in Figure 10, which shows four 500 monomer segments of four PBLG backbones constructed according to the above procedure for the time intervals $\Delta t = 0.5$ ps (i.e. the entire backbone fragment consists of a total of 8657 monomers), 1.0 ps (4329 monomers), 1.5 ps (2882 monomers), and 2 ps (2161 monomers).

To determine the unit vector $\tilde{u}$ tangential to the molecular contour, we approximate a short section of the backbone containing 6 monomers by an enveloping cylinder, which is schematically shown in Figure 9. The vector $\tilde{u}$ is then given by the normalized eigenvector corresponding to the smallest eigenvalue of the cylinder's moments of inertia tensor. We obtain the correlation function $\langle \tilde{u}(0)\tilde{u}(s) \rangle$ by averaging over all products $\tilde{u}(r)\tilde{u}(r + s)$, where r is a reference point shifted along the backbone.

Figure 11A shows a plot of $\ln \langle \tilde{u}(0)\tilde{u}(s) \rangle$ versus s for the above four high molecular weight fragments constructed for $\Delta t = 0.5$, 1.0, 1.5, and 2 ps. It is worth noting that the curves show no systematic behavior depending on the value of Δt, indicating that the conformational statistics of the constructed backbone fragments is not significantly biased due to time correlations between extracted 9-mers. Note also in this context that Δt is only the minimum time difference between two adjacent 9-mers along the constructed backbone. In general, the time difference of neighboring 9-mers may be as large as the entire length of the simulation. In fact the insert in Figure 11A shows the randomness of the "time position" of the nth 9-mer along the constructed backbone (for $\Delta t = 1$ ps) plotted versus n.

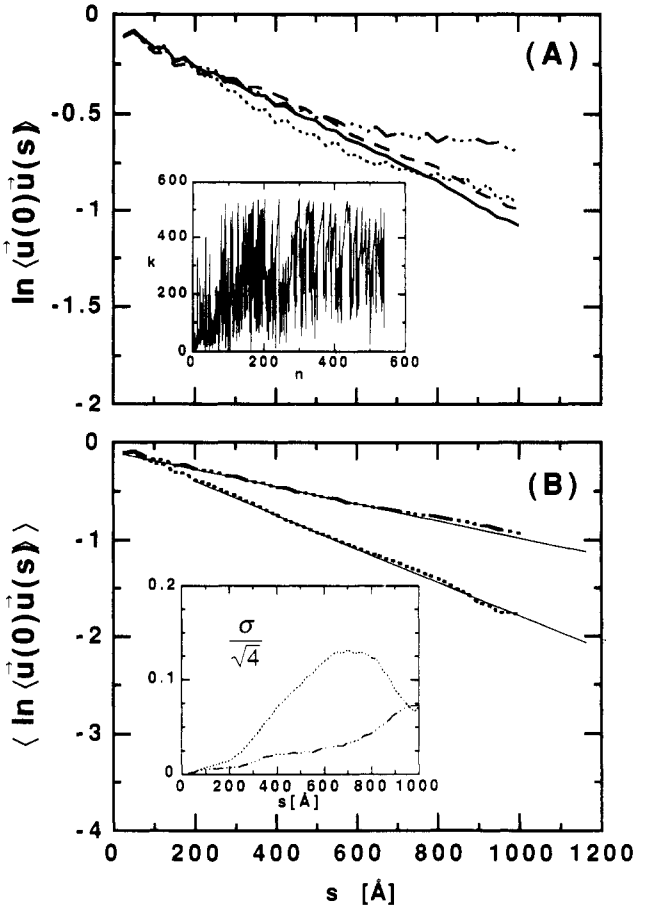

Figure 11. (A) $\ln \langle \tilde{u}(0)\tilde{u}(s) \rangle$ as a function of the distance s along the contour based on the full length fragments of which subsections are shown in Figure 10: $\Delta t = 0.5$ ps (solid line), $\Delta t = 1.0$ ps (dotted line), $\Delta t = 1.5$ ps (dashed-dotted line), and $\Delta t = 2.0$ ps (dashed line). The insert illustrates the quasi random relation between the kth 9-mer extracted from the trajectory (here $\Delta t = 1.0$ ps) and its position n along the chain of 9-mers forming the high molecular weight fragment of the PBLG backbone. (B) Average of the curves in panel A (dash-dotted line) as well as the corresponding average obtained for a vacuum simulation (dotted line). The linear fits (solid lines) are based on the data for $s \leq 600$ Å. The insert shows the error bar $\sigma/\sqrt{4}$ for the above averages as a function of s for both the solvent (dashed-dotted line) and the vacuum simulation (dotted line).

The upper curve in Figure 11B is the average of the curves in panel A, which we fit by a straight line, where the fit is based on the interval $s < 600$ Å. The slope of this line is $-1/P$ with $P \approx 1000$ Å. The corresponding error bar $\sigma/\sqrt{4}$ is shown as an insert, where $\sigma(s) = ({}^1/_4\sum_{i=1}^4[x_i(s) - \bar{x}(s)]^2)^{1/2}$ with $\bar{x}(s) = {}^1/_4\sum_{i=1}^4 x_i(s)$ and $x_i(s)$ denotes $\ln \langle \tilde{u}(0)\tilde{u}(s) \rangle$ at Δt_i $(i = 1, ..., 4)$. The increase of $\sigma(s)$ partially results from the worsening statistics for large s and, to a large extent, from the diminishing quality to which the smoothness condition is fulfilled due to the lack of suitable 9-mers. Thus we finally obtain $P = 1000 \pm 50$ Å, which is well within the range $700 < P < 1400$ Å reported for the PBLG/DMF system in the literature.[13] With vacuum as "solvent" a completely analogous calculation yields $P = 600 \pm 150$ Å. Thus even though there is significantly more scatter in this case, the calculations demonstrate that the presence of solvent molecules affects the stiffness of the helix significantly. The fact that the solvent molecules are packed around the helical backbone with a reduced mobility appears to inhibit the undulatory motion of the PBLG backbone. This results in a larger persistence length as in the vacuum case, where the backbone dynamics is apparently less inhibited.

Finally, it is worth mentioning that if the PBLG molecule is treated as a homogeneous bend-elastic thin cylindrical rod, its persistence length P is related to its Young's modulus E_R via the relation $P = \zeta/(k_BT)$[34] (we use E_R to distinguish it from the above bulk modulus E). Here ζ is a bending force constant defined via

$$V = \frac{1}{2}\zeta \int_{\text{contour}} \left(\frac{\partial \tilde{u}}{\partial s}\right)^2 ds \tag{11}$$

where V is the potential energy of the rod. According to the theory of elasticity for isotropic media ζ is given by $\zeta = E_R I$, where I is the moment of inertia of the cross section of the rod, i.e. $I = (\pi/64)D_R^4$, and D_R is the diameter of the rod.[35] Thus P is given by

$$P = \frac{\pi}{64}\frac{E_R D_R^4}{k_B T} \tag{12}$$

The usefulness of this relation, i.e. the determination of P through E_R and vice versa, in the present context depends on the applicability of the theory of continuous elastic media down to submolecular dimensions and on whether there is a meaningful D_R. The former is partially implied by the above treatment of PBLG as a persistent flexible chain. The latter we can check by inserting eq 9 into eq 12, where A is now equal to $(\pi/4)D_R^2$, which yields

$$P = \frac{1}{16}\frac{D_R^2 kL}{k_B T} \tag{13}$$

For a vacuum persistence length of 600 Å, $L = 27$ Å, $k = 34$ kcal/(mol Å^2), and $T \sim 300$ K we obtain $D_R \sim 2.5$ Å. If we take this seriously, then the effective elastic diameter D_R is mainly determined by the backbone diameter of ~4 Å (cf. Figure 2A).

Conclusion

In this work we have studied the structure and some dynamic aspects of the complex interface between an isolated "hairy rod", i.e. PBLG, and the surrounding solvent, i.e. DMF, using molecular dynamics simulations. We find that in the range where the solvent overlaps with the side chains, the solvent is highly structured; i.e. the mixing with the flexible side chains does not lead to a completely washed out solvation zone, as one might expect. Even though the simulations are for a single PBLG segment, the results may provide useful insight at high concentrations also. This is because the thermodynamic behavior of PBLG and similar polypeptides at high concentrations is to a large extent explainable by models considering only the mixing of side chains with solvent,[9] whose reliability, however, depends significantly on the radial solvent and side chain profile.

In addition, we have also investigated the elastic behavior of PBLG in DMF with the emphasis on determination of the persistence length. Here we show that the simulated molecular dynamics conformations of a comparatively short helix segment hold enough statistical information to calculate the large persistence length with considerable accuracy, which makes this technique a true alternative to the experiment. In this context it would be also interesting to apply this method to polyelectrolytes like DNA, where the persistence length has an electrostatic contribution, in addition to the intrinsic persistence length (even though intrinsic, as we have shown, includes the solvent shell). There is still some controversy with regard to the scaling dependence of this electrostatic part of the persistence length on the ionic strength.[36] Thus an atomistic computer simulation similar to the above may provide useful insight. Clearly, however, it is the long range of the Coulombic interactions, which makes this also a difficult task.

Acknowledgment. The authors wish to acknowledge several useful discussions with Prof. G. Wegner during the course of this work.

References and Notes

(1) Kubo, K.; Ogino, K. *Mol. Cryst. Liq. Cryst.* **1979**, *53*, 207.
(2) Kubo, K. *Mol. Cryst. Liq. Cryst.* **1981**, *74*, 71.
(3) Livolant, F.; Bouligand, Y. *J. Phys. (Paris)* **1986**, *47*, 1813.
(4) Lee, S. D. Ph.D. Thesis, Brandeis University, 1988.
(5) Lee, S. D.; Meyer, R. B. *Liq. Cryst.* **1990**, *7*, 451.
(6) Hentschke, R. *Macromolecules* **1990**, *23*, 1192.
(7) DuPré, D. B.; Yang, S. *J. Chem. Phys.* **1991**, *94*, 7466.
(8) Mathauer, K.; Vahlenkamp, T.; Frank, C. W.; Wegner, G. Poster presented at the ACS Spring Meeting (Division of Colloid and Surface Chemistry), Denver, 1993.
(9) Flory, P. J.; Leonard, W. J., Jr. *J. Am. Chem. Soc.* **1965**, *87*, 2102.
(10) Hentschke, R.; Herzfeld, J. *Phys. Rev. A* **1991**, *44*, 1148.
(11) Israelachvili, J. N. *Intermolecular and Surface Forces*; Academic Press: New York, 1992.
(12) Ray, D. C.; Lee, B. K.; Parsegian, V. A. *Proc. Natl. Acad. Sci. U.S.A.* **1984**, *81*, 2621.
(13) Schmidt, M. *Macromolecules* **1984**, *17*, 553.
(14) Bamford, C. H.; Hanby, W. E.; Happey, F. *Proc. R. Soc. London, A* **1951**, *205*, 30.
(15) Bamford, C. H.; Elliot, A.; Hanby, W. E. *Synthetic Polypeptides*; Academic Press: New York, 1956.
(16) Corey, R. B.; Pauling, L. *Proc. R. Soc. London, B* **1953**, *141*, 10.
(17) INSIGHT, Vers. 2.0. Biosym Technologies, 1989.
(18) Allen, M. P.; Tildesley, D. J. *Computer Simulation of Liquids*; Oxford University Press: Oxford, U.K., 1992.
(19) Techniques of Chemistry. *Organic Solvents*, 4th ed.; John Wiley & Sons: New York, 1986; Vol. II.
(20) Weiner, S. J.; Kollman, P. A.; Nguyen, D. T.; Case, D. A. *J. Comput. Chem.* **1986**, *7*, 230.
(21) Jung, B. *Simulation der Kettenkonformation von Polymeren mit Hilfe der Konzepte der Molekulardynamik-Rechnungen*, Dissertation, Johannes Gutenberg Universität, Mainz, 1989.
(22) Rappé, A. K.; Goddard, W. A. *J. Phys. Chem.* **1991**, *95*, 3358.
(23) POLYGRAF, Vers. 3.0. Molecular Simulations, Inc., 1992.
(24) Baldwin, M. A.; Welham, K. J. *Org. Mass Spectrom.* **1988**, *23*, 425.
(25) van Gunsteren, W. F.; Berendsen, H. J. C. *Mol. Phys.* **1977**, *34*, 1311.
(26) van Gunsteren, W. F.; Karplus, M. *Macromolecules* **1982**, *15*, 1528.
(27) Berendsen, H. J. C.; Postma, J. P. M.; van Gunsteren, W. F.; DiNola, A.; Haak, J. R. *J. Chem. Phys.* **1984**, *81*, 3684.
(28) Easteal, A. J.; Woolf, L. A. *J. Chem. Soc., Faraday Trans. 1* **1985**, *81*, 2821.
(29) Donohue, J. *Proc. Natl. Acad. Sci. U.S.A.* **1953**, *39*, 470.
(30) Jackson, C. L.; Shaw, M. T.; Aubert, J. H. *Polymer* **1991**, *32*, 221.
(31) Hiltner, A.; Anderson, J. M.; Borkowski, E. *Macromolecules* **1972**, *5*, 446.
(32) Landau, L. D.; Lifschitz, E. M. *Statistical Physics*, 3rd ed.; Pergamon: Oxford, U.K., 1980; Part 1.
(33) Flory, P. J. *Statistical Mechanics of Chain Molecules*; Hanser: New York, 1988.
(34) Yamakawa, H. *Modern Theory of Polymer Solutions*; Harper and Row: New York, 1971.
(35) Landau, L. D.; Lifschitz, E. M. *Elastizitätstheorie*; Akademie-Verlag: Berlin, 1975.
(36) Schmidt, M. *Macromolecules* **1991**, *24*, 5361.